Laakko, Timo; Korkealaakso, Antti; Yildirir, Burcu Firatligil; Batys, Piotr; Liljeström, Ville; Hokkanen, Ari; Nonappa; Penttilä, Merja; Laukkanen, Anssi; Miserez, Ali; Södergård, Caj; Mohammadi, Pezhman

Accelerated Engineering of ELP-Based Materials through Hybrid Biomimetic-De Novo Predictive Molecular Design

Published in:
Advanced Materials

DOI:
10.1002/adma.202312299

Published: 11/07/2024

Document Version
Publisher's PDF, also known as Version of record

ADVANCED MATERIALS
www.advmat.de

Accelerated Engineering of ELP-Based Materials through Hybrid Biomimetic-De Novo Predictive Molecular Design

*Timo Laakko, Antti Korkealaakso, Burcu Firatligil Yildirir, Piotr Batys, Ville Liljeström, Ari Hokkanen, Nonappa, Merja Penttilä, Anssi Laukkanen, Ali Miserez, Caj Södergård, and Pezhman Mohammadi**

Efforts to engineer high-performance protein-based materials inspired by nature have mostly focused on altering naturally occurring sequences to confer the desired functionalities, whereas de novo design lags significantly behind and calls for unconventional innovative approaches. Here, using partially disordered elastin-like polypeptides (ELPs) as initial building blocks this work shows that de novo engineering of protein materials can be accelerated through hybrid biomimetic design, which this work achieves by integrating computational modeling, deep neural network, and recombinant DNA technology. This generalizable approach involves incorporating a series of de novo-designed sequences with α-helical conformation and genetically encoding them into biologically inspired intrinsically disordered repeating motifs. The new ELP variants maintain structural conformation and showed tunable supramolecular self-assembly out of thermal equilibrium with phase behavior in vitro. This work illustrates the effective translation of the predicted molecular designs in structural and functional materials. The proposed methodology can be applied to a broad range of partially disordered biomacromolecules and potentially pave the way toward the discovery of novel structural proteins.

1. Introduction

Taking inspiration from high-performance protein-based structural biomaterials has led to the development of advanced functional materials.[1–5] A key aspect in molecular biomimetics of such structural proteins has been to artificially replicate their primary sequences,[5–9] often followed by randomized or rational modifications of the sequences toward desired functionalities.[10–12] While sequence information provides the foundation for our understanding of the structure-function relationships, this task is very challenging for proteins with tandem repeat motifs that tend to be partially disordered.

Typically, such proteins contain an ensemble of dynamically reconfigurable conformations that lack defined secondary structures, making them challenging to be probed both in silico and in vitro. In contrast, regions with well-defined and conformational switchable structures (e.g., α-helical $\rightarrow$ β-sheet) critically impart the biofabrication and properties of biological materials.[13,14] Considering that these relatively short α-helical motifs are in a metastable state, their intercellular expression, extracellular secretion, storage, and processing must be under strict control of physiochemical processes to prevent their premature conformational conversion.[5,15–18] This highlights that predicting functionality of structural proteins transcends beyond the linear sequence but

T. Laakko, A. Korkealaakso, A. Hokkanen, M. Penttilä, A. Laukkanen, C. Södergård, P. Mohammadi
VTT Technical Research Centre of Finland Ltd.
VTT FI-02044, Finland
E-mail: Pezhman.mohammadi@vtt.fi

B. F. Yildirir, Nonappa
Faculty of Engineering and Natural Sciences
Tampere University
Korkeakoulunkatu 6, Tampere FI-33720, Finland

P. Batys
Jerzy Haber Institute of Catalysis and Surface Chemistry
Polish Academy of Sciences
Niezapominajek 8, Krakow PL-30239, Poland

V. Liljeström
Department of Applied Physics
School of Science
Aalto University
Aalto FI-00076, Finland

A. Miserez
Center for Sustainable Materials (SusMat)
School of Materials Science and Engineering
Nanyang Technological University (NTU)
Singapore 637553, Singapore

A. Miserez
School of Biological Sciences
NTU
Singapore 637551, Singapore

The ORCID identification number(s) for the author(s) of this article can be found under https://doi.org/10.1002/adma.202312299

DOI: 10.1002/adma.202312299

also on processing conditions governing key aspects of protein behavior, such as folding, assembly, and phase behavior. Collectively, these phenomena regulate the functional and mechanical performance of protein materials.

Replicating these well-regulated physico-chemical conditions in laboratory setups is challenging. Thus, artificially produced structural proteins may be unstable and result in inferior properties compared to their native counterparts. One innovative approach that could overcome this challenge is de novo design assisted by machine learning approaches and advanced computational modeling.[19,20] Having the capability to design arbitrary sequences de novo and simultaneously predict their structures using first principles in a high throughput fashion may provide a wide range of protein materials with emerging properties.[21–23] In this paradigm, sequence and structural motifs could be guided from the bottom-up to reach specific functions by taking advantage of the entire protein sequence space to avoid instability constraints for recombinant production of structural proteins in vitro while maintaining the motif's functionality. To address these constraints, we advocate for the adoption of a hybrid biomimetic/de novo design strategy. This approach allows us to combine the strengths of both biomimicry – drawing inspiration from nature's solutions– with de novo design, enhancing our ability to engineer materials with tailored functionalities that may have been elusive otherwise.

Accordingly, here we outline a rapid targeted design workflow for predicting de novo design α-helices inspired by tropoelastin's poly-alanine domain but with greater molecular stability.[24] We used multiscale computational modeling (MCM) and CNN (Convolutional Neural Network) deep neural network models (**Figure 1**) to select the best-performing designs for experimental production by encoding them into intrinsically disordered pentapeptide motifs of tropoelastin and produced recombinantly as guest motifs. The resulting elastin-like polypeptide (ELP) variants exhibited tunable self-assembled structures and phase behavior, both in silico and in vitro. We demonstrated that phase separation behavior can be precisely controlled in two stages: initially through the use of distinct de novo design of α-helices motifs, and subsequently through the adjustment of formulation parameters. Some variants were used as programmable thermoresponsive injectable matrices and transmittance modulators for smart windows.

2. Results

2.1. Learning the Grammar of Elastin's Ordered-Disordered Sequences

Tropoelastin, the precursor building block of elastin,[25,26] shares noticeable similarities with other high-performance protein-based fibrous materials (Figure S1, Supporting Information).[5,27] At the sequence level, it is highly repetitive and consists of unstructured hydrophobic motifs (≈80%, Table S2, Supporting Information) interspersed by structured hydrophilic modules (≈20%, Figure S1, Supporting Information).[5,28] The hydrophobic regions comprise of di-, tri-, penta-, and hexa-peptide repeats enriched in proline (Pro), glycine (Gly) and valine (Val) (Table S2, Supporting Information)[5,27,29] amino acids that favor transient fluctuations and structural disorder. In contrast, the hydrophilic regions are dominated by alanine (Ala) and lysine (Lys) residues arranged as conserved 12 to 21 residues long blocks that adopt α-helical conformations (Table S2 and Figure S2, Supporting Information)[5,28] Cross-linking subsequently occurs within the core of these helices. Overall, unstructured regions interspersed by cross-links confer a high degree of mechanical elasticity and recoil to tissues made of elastin.[12,30] The incorporation of structured domains also contributes to the liquid-liquid phase separation (LLPS) of tropoelastin (also called coacervation).[28,31,32] While the unstructured regions alone are sufficient to form a colloidal suspension of µm-sized liquid-like coacervates, the introduction of helices decreases the free energy of the system during LLPS mediated by water exclusion, self-association, and increased intermolecular interactions.[12,30]

2.2. Creating a Library of de novo Designed α-Helical Domains

The AI-empowered material scientist (AIMS) protocol predicted 1800 novel helices (Figure 1) based on the criteria of having a length ranging from 20 to 40 residues (Figure S3, Supporting Information). Using the helix propensity feature map, candidates were strained to 178 AIMS predicted helices (AI.PH$_n$, n = identification number of the helix), with a score above 0.7, while the rest were excluded from further analysis (Figure 1a). Additionally, we excluded 34 candidates based on the AIMS prediction accuracy score bellow 0.8, and those that exhibited the average root mean square deviation (RMSD) above 3 Å after two-step atomistic molecular dynamic (MD) simulation (Figure 1b–d). Ultimately, from the pool of 144 de novo sequences, 25 variants were selected each with distinct physicochemical features for recombinant expression (Figures S4–S6, Supporting Information). The complete list of selected variants is provided in Table S1, Supporting Information. Of the set, 13 of the 25 were grouped as alanine-rich AI.PH$_n$ due to the abundance of alanine resembling naturally occurring motifs (Figures S4–S6, Supporting Information). To understand the potential roles and interactions of these peptides, a classification framework was developed based on amino acid composition, sequence motifs, and specific residues, hypothesizing varied physicochemical properties and functions. These sequences presented are predominantly characterized by a high occurrence of alanine and isoleucine, with sporadic appearances of other amino acids such as glycine, aspartic acid, lysine, and others, contributing to their unique properties. The alanine-rich sequences, including AI.PH$_4$, AI.PH$_8$, AI.PH$_{36}$, AI.PH$_{48}$, AI.PH$_{70}$, AI.PH$_{97}$, AI.PH$_{123}$, and AI.PH$_{177}$, highlight alanine's propensity for alpha-helix formation, suggesting these sequences may favor such secondary structures. In tandem, the alanine-isoleucine sequences from the same set emphasize a blend of helix-forming and hydrophobic characteristics due to the presence of isoleucine, hinting at their potential structural stability and interaction with hydrophobic environments. The inclusion of aspartic acid in sequences AI.PH$_{45}$, AI.PH$_{87}$, AI.PH$_{142}$, and AI.PH$_{162}$ introduces acidic traits, which might influence their solubility and molecular interaction. These sequences, along with unique residues like tyrosine, phenylalanine, and histidine, fall into the special feature sequences category, suggesting specialized functionalities. Last, the

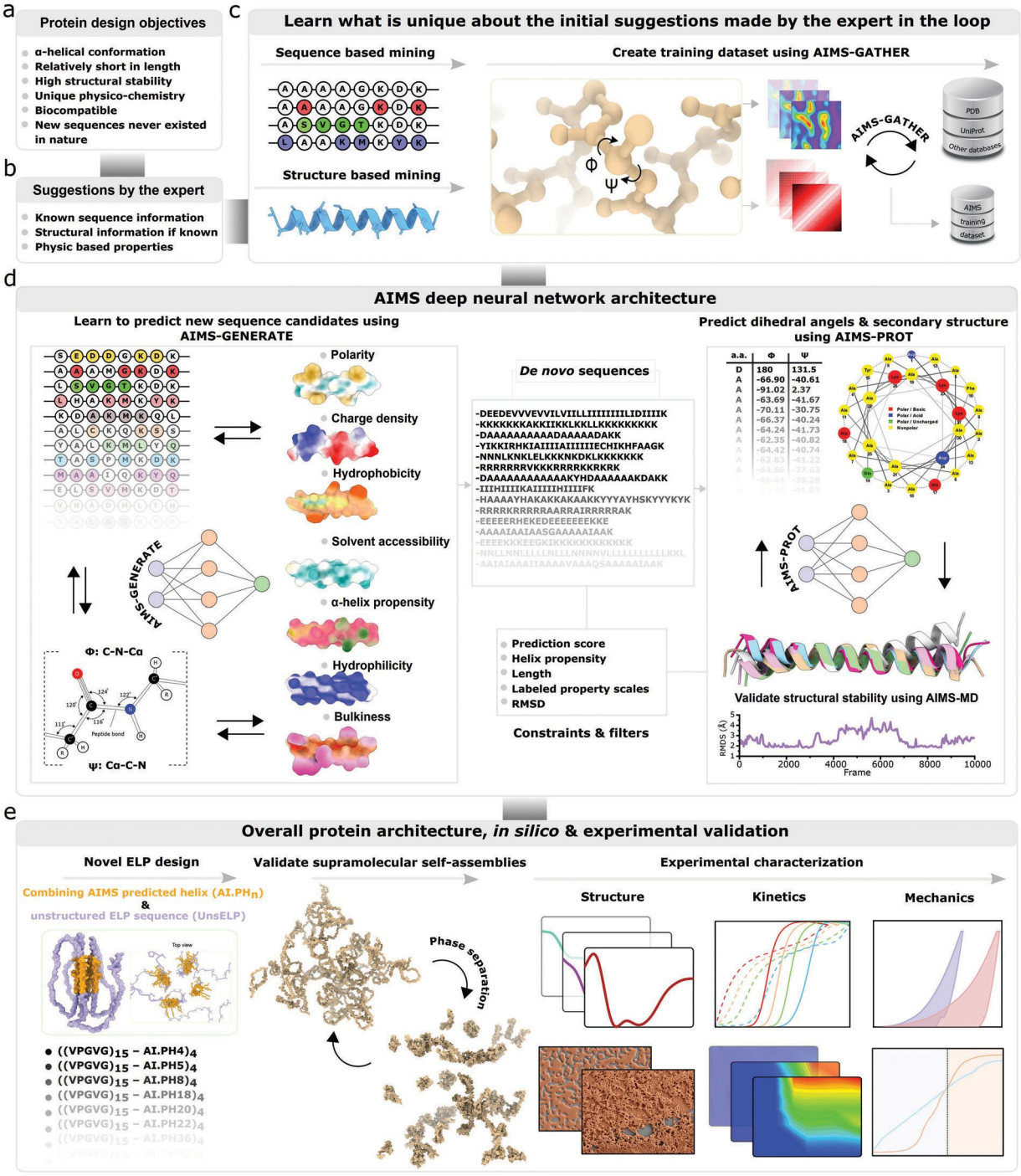

Figure 1. Overview of the AI-empowered material scientist (AIMS) protocol for generating hybrid biomimetic – de novo designed elastin-like polypeptides (ELP) and their use in protein-based-material engineering. The flowchart includes a) α-helix design objectives and b) suggestions from the human in the loop. c) AIMS-GATER carries out data mining to identify homologous templates based on provided sequences or structural information of elastin's α-helical motifs. The hydrogen bond estimation algorithm (DSSP) is used to compute the relevant structural confirmation if there are no secondary structure homologs for the suggested sequences. From all the obtained models, conformationally sensitive dihedral geometrical angles (Ψ and Φ angle) are calculated. d) As an input, the corresponding 2D inter-residue angular torsion is fed into the deep neural network as the training set, until the hidden correlation between the sequence, dihedral angles, and labeled property scales become visible that guides the subsequent step of the generation of completely new helices followed by predicting their dihedral angles. Structural stability for all newly predicted helices is assessed using atomistic molecular dynamic simulation in a two-step procedure of energy minimization and relaxation. e) Best performing AIMS predicted helices (AI.PH$_n$) is selected by the expert in the loop based on the desired properties and the required functionalities. Selected helices are incorporated within an unstructured region of an elastin-like polypeptide (UnsELP), yielding full-length hybrid proteins (see Methods and Table S1, Supporting Information). Different in silico and in vitro tests are performed to validate the supramolecular self-assembly, structure, kinetics, and mechanics of the hybrid proteins.

presence of glycine in sequences AI.PH$_4$ and AI.PH$_{97}$ may add flexibility, leading to their classification as flexible alanine sequences, potentially affecting their conformations and functional roles.

The remaining 12 were group alanine-less AI.PH$_n$ consists of no alanine residues. The acidic dominance sequences such as AI.PH$_{22}$, AI.PH$_{43}$, AI.PH$_{134}$, and AI.PH$_{144}$, are characterized by a high glutamic acid content, indicating strong acidity that might affect solubility and molecular interactions. Sequences AI.PH$_{64}$, AI.PH$_{102}$, and AI.PH$_{129}$, in the mixed acidic and basic sequences, shows a balance of acidic and basic residues, suggesting amphipathic properties important for electrostatic interactions. The hydrophobic-leucine-rich subgroup consists of sequences AI.PH$_5$, AI.PH$_{18}$, AI.PH$_{20}$, and AI.PH$_{46}$ highlights leucine's role in hydrophobic interactions, potentially indicating structural or self-associated functions. Sequence AI.PH$_{127}$ in the special motif subgroup, containing histidine and isoleucine, suggests unique functional capabilities. The extended lysine stretch subgroup, with AI.PH$_{102}$ and AI.PH$_{129}$, features long lysine sequences, indicating strong binding potential due to positive charges. Finally, the high glutamic-leucine mix subgroup, is exemplified by AI.PH$_{43}$, merges acidic and hydrophobic properties, indicating a complex relationship between solubility and structural roles.

2.3. Recombinant Production of Full-Length Sequences by Combining Intrinsically Disordered ELP and AI.PH$_n$

We next genetically engineered twenty-five de novo-designed ELPs variants for recombinant expression in *Escherichia coli (E. Coli)*. This was carried out by incorporating fifteen repeats of the IDP ELP sequence (VPGVG)$_{15}$,[33] followed by a single AI.PH$_n$. The tandem repeat of comprising AI.PH$_n$ and (VPGVG)$_{15}$ was then repeated four times to create the full-length hybrid protein sequences named UnsELP-AI.PH$_n$, where "*n*" corresponds to the identification number of predicted helices (Table S1, Supporting Information). Out of the 25 initially selected candidates, 15 successfully expressed the coding sequences. Of those, the 10 best-producing UnsELP-AI.PH$_n$ variants with substantially higher yields were selected and the rest were excluded (**Figure 2e** and Figures S7–S9, Supporting Information).

2.4. AIMS Predicted Sequences Showed α-Helical Conformation In Vitro

For accuracy comparison, we first predicted the atomistic models of the AI.PH$_n$ using AlphaFold2 (Figure S10, Supporting Information).[34,35] We found identical predictions comparing AIMS and AlphaFold2. Similarly, we used AlphaFold2 to predict the full-length sequences.[34,35] In all cases, AI.PH$_n$ regions were accurately predicted as α-helical and the UnsELP regions as unstructured (**Figure 3a**). To better evaluate the overall stability of the AI.PH$_n$ we performed 100 ns MD simulations (Figure 3a). All the AI.PH$_n$ maintained their conformation. By the end of the simulation, we noted most AI.PH$_n$ eventually self-associates to form di or tetramers (Figure 3a, and Figures S11–S15, Supporting Information). Experimentally measured circular dichroism (CD) from all the Hybrid biomimetic – de novo-designed ELP variants strongly exhibited α-helical conformation (Figure 3b,c). This is evident from two negative bands, at 205–210 and 220–225 nm. The predicted CD signals obtained from MD simulations also exhibited a close match (Figure 3b,c). Although the MD simulations have predicted a higher proportion of negative CD values mainly ≈205 nm for some of the variants, the overall shape and pattern of the spectra closely resemble those obtained experimentally. This consistency across the spectra supports the reliability of the in silico-derived structural conformations, while we acknowledge the limitation of the computational model in quantitatively capturing the exact extent of α-helical conformation. Furthermore, heating/cooling cycles had minimal impact on the shape of the spectra suggesting high conformational stability (Figures S16 and S17, Supporting Information). A quantitative calculation of secondary structures from CD spectra shows α-helices forming the second major conformation in all cases (up to 31%) (Figure 3d).[38] As expected, the random coils or disordered structures (indicated as "Others") formed the major overall percentage (34–48%). In contrast the predicted CD signal showed 63–80% contribution, indicating that the UnsELP may not remain completely unstructured under experimental conditions (Figure S18, Supporting Information). The UnsELP may partly adopt other conformations such as turns (<17%), distorted helices (<15%), and right twisted antiparallel β-sheets (<11%) (Figure 3d). We confirmed such arguments to be plausible after performing high-resolution Attenuated total reflection – Fourier transform infrared (ATR-FTIR) and deconvoluting the conformationally sensitive Amide-I peak (Figure 3e and Figure S19, Supporting Information). The α-helical contribution remained between 19–39%, whereas the random coil, turn, and β-strands, aggregated accounted for 40–60%.

We also collected small and wide-angle X-ray scattering (SAXS/WAXS) spectra to better understand the solution structure (Figure 3f). The SAXS data were used to generate a simulated body ab initio model via direct fitting.[36] The models were able to accurately account for the globular shape proteins present in the monodisperse form. Further analyses, including Guinier and Porod analyses, demonstrated that the data had good quality and showed no significant aggregation. For UnsELP-AI.PH45, we determined a Porod volume (V_p) of 135 746 Å^3, a radius of gyration (R_g) of 33.46 ± 0.56 Å, and a maximum dimension (D_{max}) of 108.75 Å. Subsequently, we analyzed the scattering at wider angles to probe the molecular structures Figure 3g. The WAXS diffraction patterns exhibited helical characteristics, as identified by the (100) reflection at 1.55 Å^{-1} arising from the periodicity of helices, and the (010) reflection at 0.61 Å^{-1} corresponding to the inter-helical distance. Findings were in good agreement with the simulated WAXS in solution based on explicit-solvent all-atom MD computations Figure 3g.[37] We also observed similar SAXS/WAXS spectra for the other variants (Figures S20 and S21, Supporting Information**)**. Finally, we benchmarked the conformational stability of the de novo-designed α-helical with both naturally occurring and rationally engineered α-helices and found that AI-PH$_n$ showed greater molecular stability than naturally occurring sequences (Figures S22–S26, Supporting Information).

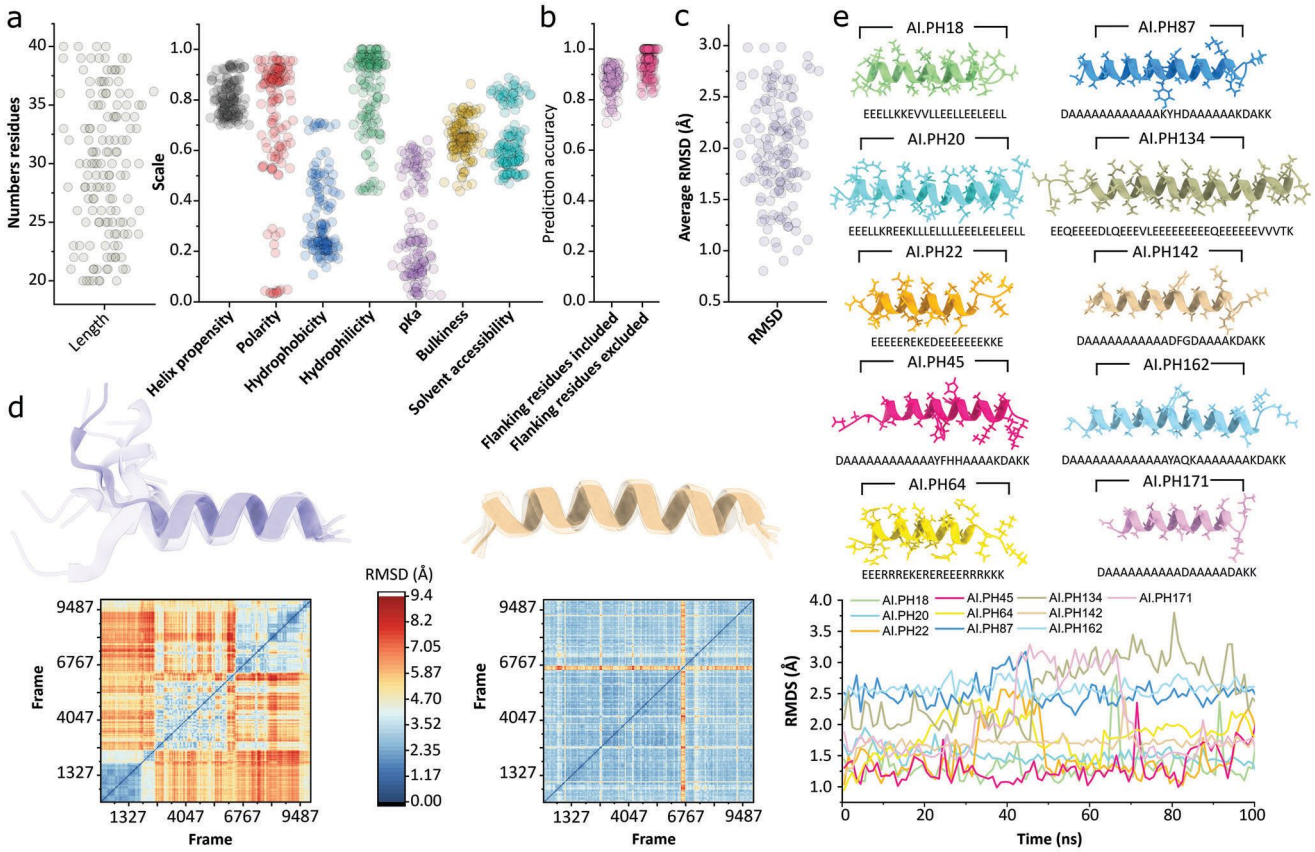

Figure 2. Screening and selection of the best performing AIMS predicted helices (AI.PH$_n$) based on desired physicochemical properties and conformational stability. a) The panels show 178 AI.PH$_n$ candidates with lengths ranging from 20–40 amino acids long and their labeled properties. Only the predicted candidates with a helix propensity score above 0.7 are shown and used in this study. b) AIMS prediction score for all the AI.PH$_n$ in the pool with or without the first and last residues at the N and C-terminus that are prone to structural fluctuation, thus lowering the overall prediction accuracy. Only AI.PH$_n$ with a prediction score of above 0.8 was selected for this study. c) To identify any structural instability within the pool, all the AI.PH$_n$ were subjected to atomistic MD simulation. Only the candidates with an average RMSD value below 3 Å were selected for further analysis after an initial 20 ns followed by an extended 100 ns simulation time. d) Representative comparison between two cases with an RMSD value above and below 3 Å. The panel also shows the overlaying conformations at various time points during MD simulations and 2D RMSD plots for each case. e) Atomistic structures of the 10 best-producing variants after 100 ns MD simulations and their corresponding RMSD profiles.

2.5. Tunable Phase Behavior and Supramolecular Self-Assembly

We explored the phase-separation response by simultaneously changing the solution conditions including the protein concentration, ionic strength, and temperature range (20 to 90 °C) for all the UnsELP-AI.PH$_n$.[39] About 1170 solution conditions were tested resulting in about 150 phase diagrams (**Figure 4a** and Figures S27–S37, Supporting Information). In all cases, the shape of the coacervation boundary was concave up-decreasing. Maximum protein and salt concentrations caused rapid turbidity shifts from clear to cloudy within seconds. Furthermore, we observed that the phase-behavior was sequence-dependent, with the following fastest to slowest condensation dynamic: UnsELP-AI.PH45 > UnsELP-AI.PH162 > UnsELP-AI.PH18 > UnsELP-AI.PH171 > UnsELP-AI.PH142 > UnsELP-AI.PH20 > UnsELP-AI.PH134 > UnsELP-AI.PH87 > UnsELP-AI.PH22 > UnsELP-AI.PH64 (Figure S38, Supporting Information). The order of the phase separation strongly correlated with the hydrophobicity of the residues and the length of the AI.PH$_n$, but inversely correlated with the polarity, hydrophilicity, and charged residues in the AI.PH$_n$ (Figures S8 and S9, Supporting Information).

To better understand the onset of assembly, we tested one concentration combination slightly above the condensation boundary (Figure 4b and Figures S39–S41, Supporting Information). In all cases, phase-separation was found to be reversible with clear solutions upon cooling (T_t-cooling). Importantly, thermal cycling phase behavior (T_t-cooling < T_t-heating) strongly correlated with the protein concentration (Figure 4c) and the traces of hysteresis curves remained identical in consecutive cycles (Figure 4d). Over the same temperature range, we monitored the dynamics of phase separation by measuring the apparent hydrodynamic diameter (d_h) using dynamic light scattering (DLS) and correlated that to the changes in the turbidity of the samples. The experimental readouts suggested condensation of the UnsELP-AI.PH$_n$ follows classical nucleation theory and relies on weak-interacting precursors (Figure S42, Supporting Information).[40]

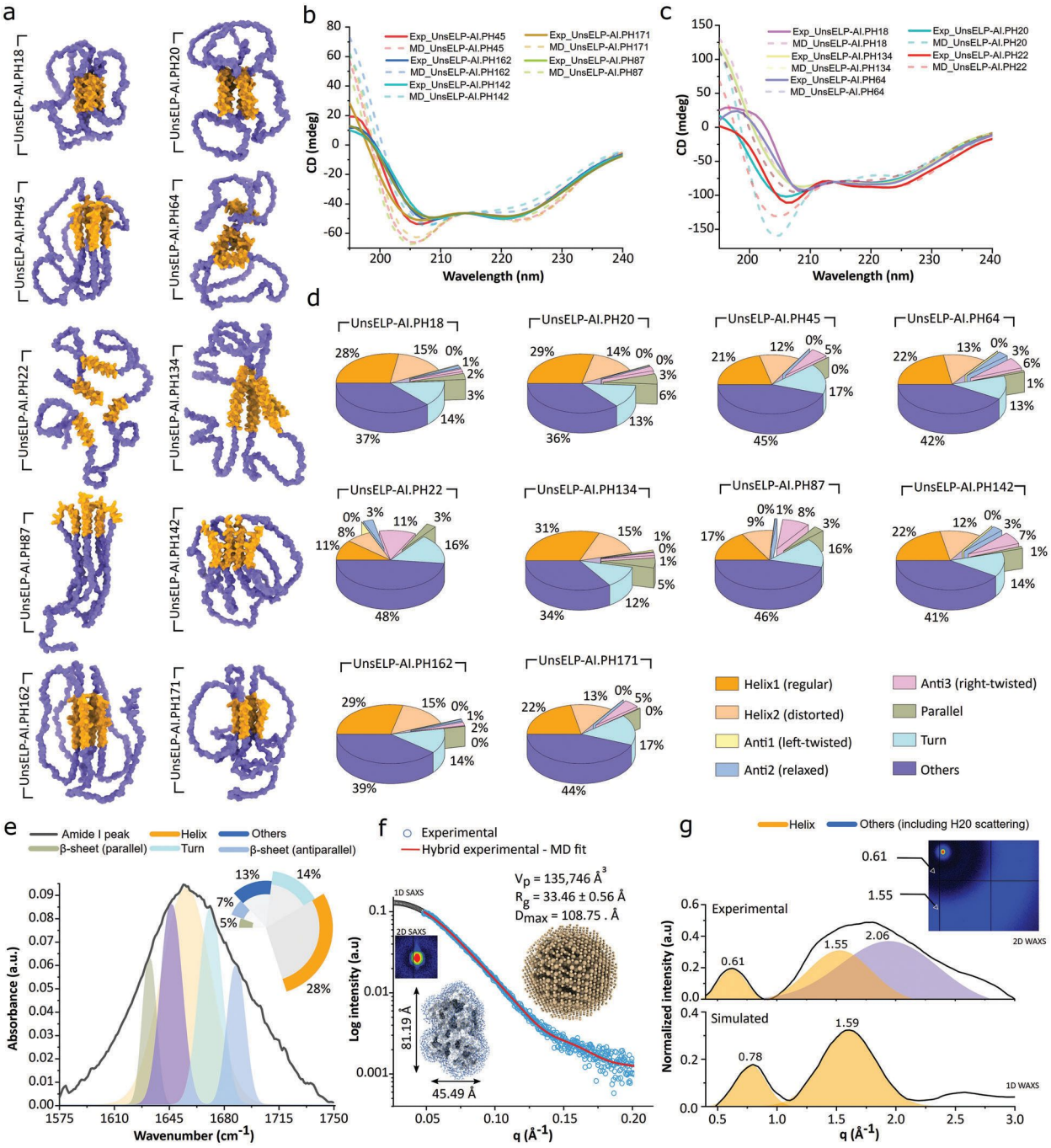

Figure 3. All the predicted de novo designs maintained their helical conformation under experimental conditions after their incorporation into the unstructured elastin-like polypeptide to make full-length hybrid proteins. a) Predicted atomistic model of ten best-producing UnsELP-AI.PH$_n$ using of Alphafold.[34,35] The orange color corresponds to AI.PH$_n$, whereas the blue color corresponds to UnsELP. b) Experimental circular dichroism (CD) spectra for the alanine-rich containing AI.PH$_n$ variants. The panel also demonstrates predicted CD signals for the corresponding models by averaging the last 100 trajectories of a 100 ns MD simulation. c) Experimental and predicted CD spectra for the alanine-less containing AI.PH$_n$ variants. d) Calculated secondary structure from experimental CD spectra for all the corresponding samples in b and c. The percentage contribution from each fold is labeled and color-coded accordingly. e) Attenuated total reflection – Fourier transform infrared spectroscopy (ATR-FTIR) spectrum and peak deconvolution identifying corresponding secondary structures of UnsELP-AI.PH45 in solution. f) 1D and 2D small angle x-ray scattering (SAXS) patterns from the UnsELP-AI.PH45. The experimental data (blue empty circles) was fitted with simulated SAXS data using the ATSAS software package indicated with the red solid line.[36] The panel also shows a low-resolution ab initio model calculated from experimental data. The atomistic model of UnsELP-AI.PH45 with the major dimensions are also indicated. g) 1D and 2D wide-angle x-ray scattering (WAXS) patterns for UnsELP-AI.PH45. The panel shows peak deconvolution with characteristic peaks corresponding to helical conformations in orange versus and unstructured region in blue, as well as the water scattering signal. The panel also shows simulated WAXS in solution based on explicit-solvent all-atom MD simulations.[37] Note: All spectral analyses, including CD, ATR-FTIR and SAXS/WAXS, were performed at a temperature of 23 °C.

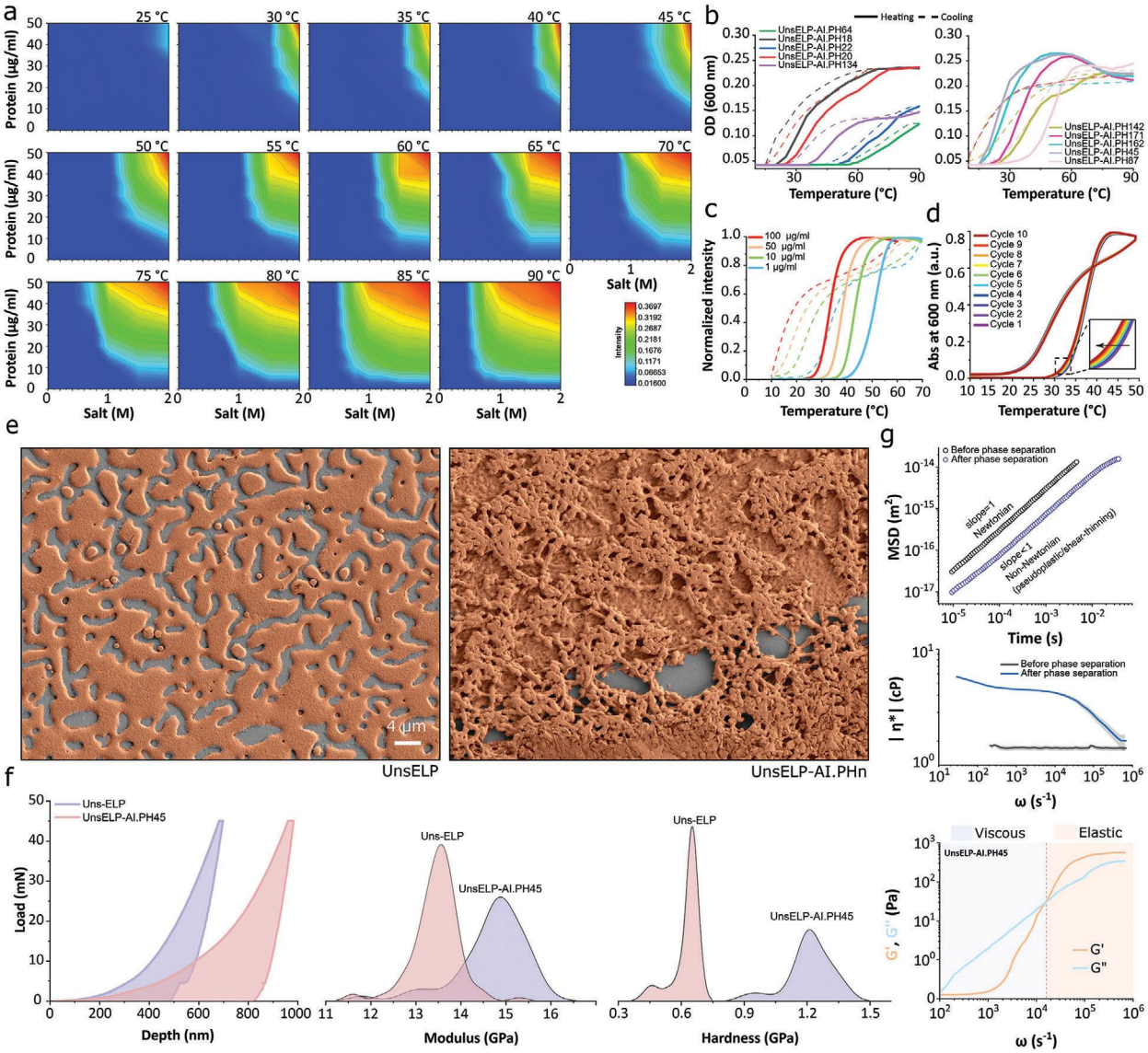

Figure 4. Sequence-dependent tunable supramolecular self-assembly, phase behavior, complex viscoelastic and mechanical properties. a) Representative LLPS diagram for the UnsELP-AI.PH171 at different protein versus salt concentrations. The diagram was constructed according to the turbidity readout at 600 nm which detects coacervation accompanying phase-separation of the protein in the solution at various temperatures ranging from 25 to 90 C° with 5 C° increments. See Figures S38–S49, Supporting Information, for the phase diagram of all the other variants. b) The optical density (OD) readout as a function of temperature exhibits sharp and reversible phase behavior. The onset of coacervation temperature, as well as coacervate dissociation (Tt-heating & Tt-cooling), directly correlate with the physicochemical properties of each AI.PH$_n$. The concentration of the protein was 50 μg mL^{-1} and the salt concentration was 2 M in all cases. c) The phase shift, Tt-heating, Tt-cooling, and ΔTt-hysteresis strongly correlate with the concentration of the protein in the solution. d) Thermal cycling (heated and cooled) of 50 μg mL^{-1} UnsELP-AI.PH171 with 2 M salt, illustrating no perceptible changes in thermal behavior and repeatable hysteresis. e) Side-by-side comparison of phase-separated full-length UnsELP versus UnsELP-AI.PH45 using high-resolution SEM images. Grayscale images were falsely colored for better visibility. f) Nanoindentation of both coacervate types after dehydration. From left to right the panel shows representative loading-unloading curves, distribution of modulus, and hardness, extracted from a hundred independent measurements (N = 100). g) The ensemble-averaged mean square displacement (MSD) of 1 μm polystyrene tracer particles (PTP) was acquired for the UnsELP-AI.PH45 with 100 μg mL^{-1} before and after the phase transition using a dynamic light scattering (DLS). The panel also shows the extracted frequency-dependent complex viscosity of the UnsELP-AI.PH45 after condensates and its frequency-dependent viscoelastic moduli before condensates. The crossover frequencies are indicated by black dashed lines. The elastic regime is shaded orange versus light blue for the viscous regime.

2.6. Reconfigurable Structural Morphology with Increased Mechanical Properties

We next studied helix-incorporated UnsELP-AI.PH$_n$ and compared it with UnsELP (Figure 4e and Figure S27, Supporting Information). Each formed distinct coacervate types with notable morphological differences. UnsELP displayed spinodal decomposition-like condensates, resembling liquid-like coacervate droplets formed after gravitational sedimentation, coalescence, and surface wetting. In contrast, UnsELP-AI.PH$_n$s

displayed highly elongated, interconnected mesoglobular porous networks with solid-like behaviors. Independent of helix type, all the UnsELP-AI.PH$_n$ qualitatively showed the same morphologies (Figure S27, Supporting Information). Fluorescence Recovery After Photobleaching (FRAP) on hydrated specimens of condensated UnsELP indicated rapid recovery, suggesting high diffusion dynamics with recovery from 0 to 80% within 30 s, followed by a marginal increase to 90% in the next 90 s (Figure S43, Supporting Information). In contrast, the UnsELP-AI.PH45 demonstrated a nearly two-fold decrease in diffusion rate, resulting in an overall recovery rate of slightly below 38% indicative of a kinetically arrested state. We also measured the mechanical properties of the constructs by nanoindentation (Figure 4f). The measurements from UnsELP showed elastic modulus, hardness, and stiffness with peak distributions of 13.4 GPa, 0.6 GPa, and 1.2×10^4, respectively, whereas UnsELP-AI.PH45 exhibited elevated properties measured at 14.9 GPa, 1.3 GPa, and 4.3×10^4, indicating that incorporating helices motifs markedly increases the mechanical properties (Figure S44, Supporting Information).

2.7. Helix-Dependent Control over Microrheological Response

We used particle tracking microrheology to investigate how AI-PH$_n$ properties affect condensate viscoelasticity near the condensation onset with rapid self-assembly kinetics (Figure 4g and Figures S45 and S46, Supporting Information).[41] This allowed us to extract frequency-dependent shear moduli up to 10^2–10^3 Pa over a broad time scale in the range 10^2–100^6 s^{-1}, which is inaccessible with conventional mechanical oscillatory microrheology ($<10^2$ s^{-1}).[41] We found that the complex viscosity of the resulting condensates is sequence-dependent and recorded zero shear viscosity ranging from 2 to 7 CP. Among all the variants, the UnsELP-AI.PH18, UnsELP-AI.PH22 and UnsELP-AI.PH87 condensates exhibited the lowest viscosity with a Newtonian fluid behavior. Furthermore, their complex modulus was found to be dominated by the viscous component (with $G' < G''$) throughout the entire frequency range ($\approx 10^2$–10^6 Hz). This was in contrast with the condensate of UnsELP-AI.PH87, UnsELP-AI.PH162, UnsELP-AI.PH20, UnsELP-AI.PH64, UnsELP-AI.PH134, UnsELP-AI.PH142, UnsELP-AI.PH45 and UnsELP-AI.PH171 exhibited greater viscosities and shear-thinning flow. Most importantly the resulting condensates highly resembled Maxwell fluids with $G' > G''$.[42] This is evident from the elastically dominant response at shorter frequencies versus liquid-like behavior at higher frequencies, with a single crossover between the two regimes (Figure 4g).[42] The stiffness of the condensate network strongly correlated with hydrophobicity, molecular weight, and length, while inversely correlating with polarity and hydrophilicity (Figure S47, Supporting Information).

2.8. A Multitude of Molecular Interactions Govern the Intricate Process of LLPS

To delve deeper into the complex dynamics of LLPS, we conducted all-atom molecular dynamics (MD) simulations based on experimental findings (**Figure** 5a–d, and Figures S48–57, Supporting Information). Due to limitations in simulating full-length sequences, we used a single repeat from UnsELP-AI.PH$_n$ (Table S3, Supporting Information). We found that phase-separation relied on several molecular interactions, including hydrophobic, van der Waals, $\pi-\pi$, cation-π, and hydrogen bonding for almost all the variants but also electrostatic interactions in some cases (Figure 5b). These interactions facilitate higher-order structural organization mainly between helix-helix and helix-coil, but also coil-coil domains.[28,43] At the start of the simulation, oligomers were well-solvated and dispersed below the critical LLPS temperature (Figure 5a). At increasing temperature, they began to inter-associate and form clusters that coalesced into larger assemblies, particularly noticeable for UnsELP-AI.PH45. Above the transition temperature, the spherical clusters transformed into denser rod assemblies due to dehydration-induced collapse. This reduced their solubility and surface area requirements, making them less dynamic and reaching equilibrium by the end of the simulation (Figure 5a). The Na^+ and Cl^- ions tend to further promote this effect by hindering interfacial interactions network between water molecules and the UnsELP-AI.PH45 (Figure 5c). The change in the balance between entropic costs and enthalpic gains arising from this collapse tends to drive a thermodynamic preference for elongated rod-like structures similar to the experimental findings, unlike UnsELP adapting a more spherical conformation (Figures S27 and S56, Supporting Information).[44] Factors such as length, amino acid sequence, and domain composition can influence the preference for rod-like assemblies as qualitative differences among the variants were observed **in** Figures S48–S57, Supporting Information. We also observed that AI.PH$_n$ acted as a sticky domain and formed a stapler unit between proteins. To understand enthalpic stabilization, we looked into free energy calculations focusing solely on profiling helix-helix homodimerization, omitting helix-coil and even coiled-coil due to structural instability (Figure 5d and Figure S55, Supporting Information). The results indicated that the association of two helices was highly energetically favorable, with the minimum of the association profile between 0.5 – 1.5 nm corresponding to ΔG_{assoc} ranging from −5 to −75 kJ mol^{-1}. ΔG_{assoc} for all constructs is provided in Table S3, Supporting Information. Finally, no significant free energy barriers was observed for helix-helix complexation and there was only one global free energy minimum, indicating that the helices were fully associated and maintained inter-helical contact along their longest dimension.

2.9. Material Engineering and Application of Biomimetic – de novo Designed ELPs

We envision the use of the UnsELP-AI.PH$_n$ in a variety of high-added-value biomedical and industrial applications. As a first proof-of-concept, we carried out in vitro cytocompatibility assessment by culturing various mammalian cell types on the surface of glass substrates coated with either UnsELP-AI.PH45, UnsELP-AI.PH87, UnsELP-AI.PH22 or UnsELP-AI.PH64 (**Figure** 6a,b). We found no significant differences between the variants used for coating the substrates. All cases could support cell adhesion, growth, and proliferation with no apparent cytotoxicity in comparison to uncoated tissue culture plates (TCP) indicative of their potential use for biomedical applications. Considering UnsELP-AI.PHn's capacity to phase transition into stable viscoelastic

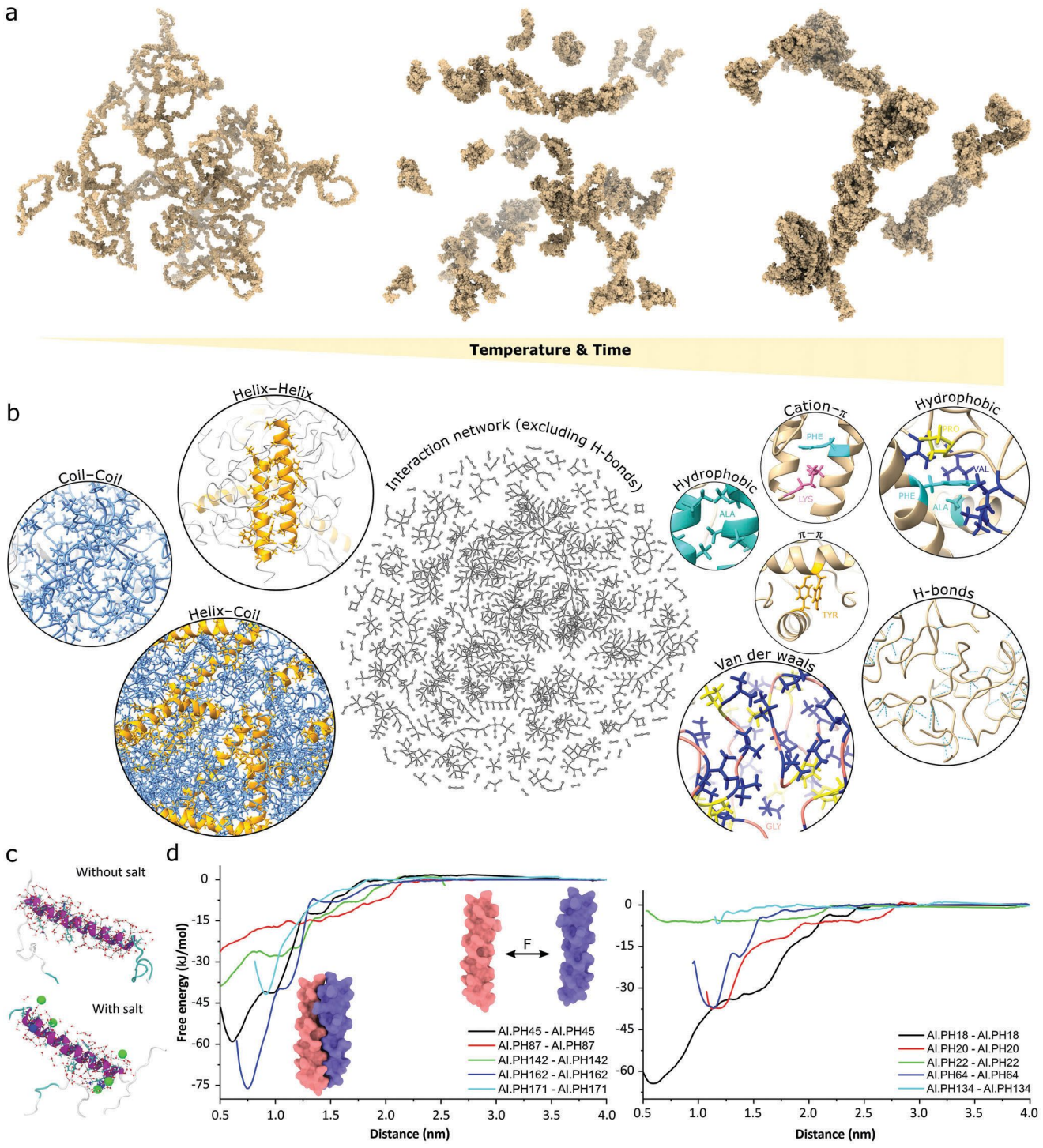

Figure 5. Large-scale molecular dynamics (MD) simulations of UnsELP-AI.PH$_n$ phase separation. a) All-atom explicit solvent system (water, Na^+, and Cl^-) composed of 50 single repeats of UnsELP-AI.PH$_{45}$ with temperature ramp from 5 to 50 °C with 15 °C increment for every 50 ns. The panel shows snapshots taken throughout the length of the simulation to demonstrate the evolution of condensation as the temperature reaches and exceeds the LCST over time. b) A closer inspection of the simulation reveals the multitude of molecular interactions. These include hydrophobic, van der Waals, π–π, cation- π, and hydrogen bonding that facilitates higher-order structural organization between helix-helix, helix-coil, and helix-coil domains. c) Visual representation for obstruction of the interactions between water molecules and the AI.PH45 in the presence of Na^+ and Cl^-. d) Free energy profile of transient dimerization of helix-helix homodimers.

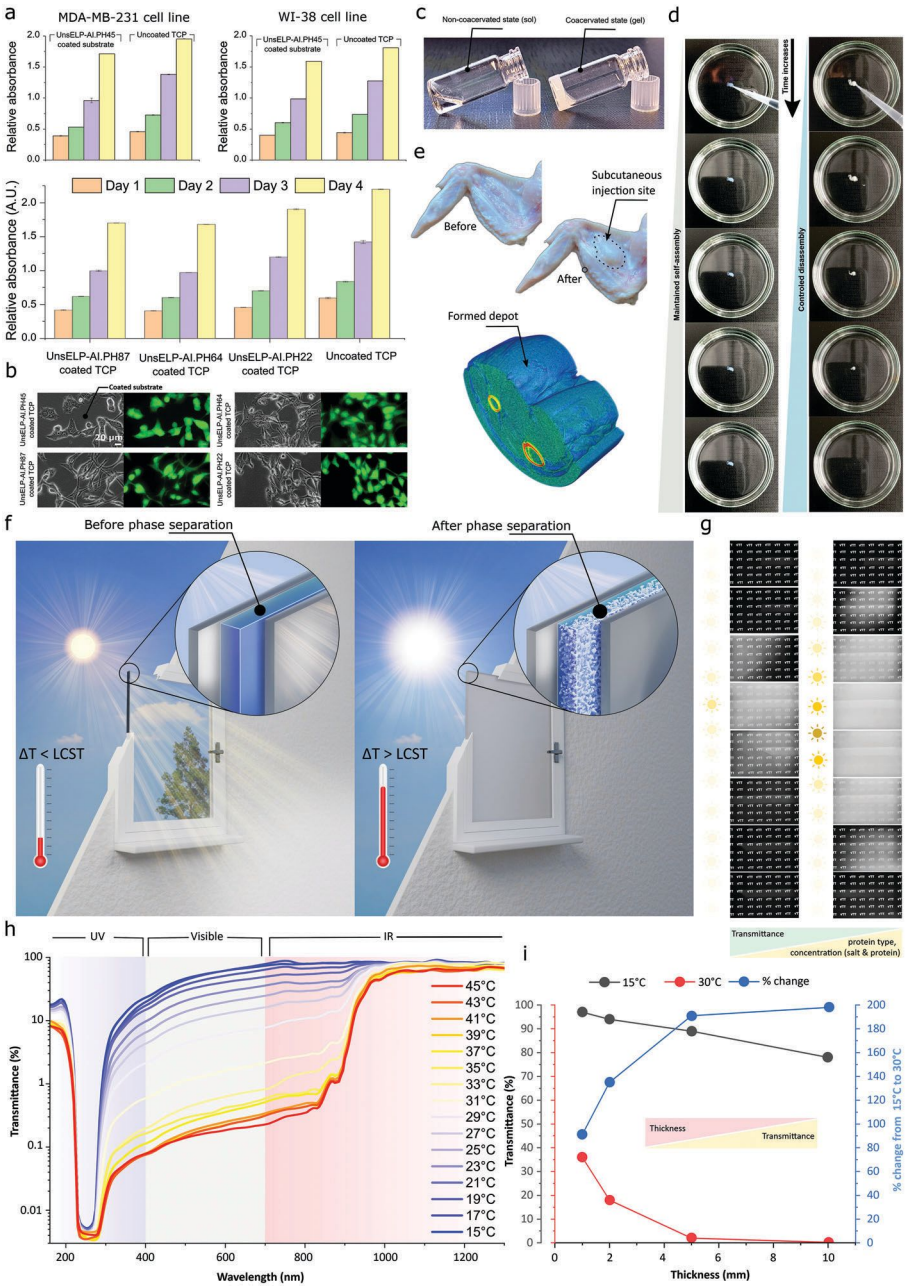

Figure 6. Material engineering and application of phase-separated UnsELP-AI.PH$_n$. a) CCK-8 (WST 8) cytotoxicity assay of WI-38 and MDA-MB-231 cell lines cultured for 4 days on substrates coated with UnsELP-AI.PH45 (N = 3 in all cases). Uncoated tissue culture plates (TCP) were used as controls. No significant difference could be found between the coated and uncoated surfaces. The panel also shows representative phase contrast and fluorescence images of the MDA-MB-231 cultured on the coated substrate. b) Cytotoxicity assays for coated surfaces with UnsELP-AI.PH87, UnsELP-AI.PH64 and UnsELP-AI.PH22 variants. The plot only shows the result for the MDA-MB-231 cell line. c) The panel shows programmable depots made from UnsELP-AI.PH45. The reservoir on the left represents a non-coacervated formulation, whereas the one on the right shows the coacervated state. d) The series of images on the left represent a depot with maintained self-assembly (first image T = 0 min, and last image T = 71 min), whereas on the right a depot with controlled disassembly (first image T = 0 min, and last image T = 2.3 min) corresponds to the non-coacervated and coacervated formulations shown in c, respectively. e) Stability and tissue incorporation test of UnsELP-AI.PH45 by making injections into the wingette's subcutaneous space of a sacrificed domestic chicken. The injection site is indicated with a solid circle and the area around the depot with a dashed line. The panel also shows X-ray computed microtomography (Micro-CT) from the site of injection. f) Schematic representation of the transmittance modulation of smart windows for solar light and heat regulating. The concept relies on the formation of a reversible anisotropic interconnected mesoglobular network of UnsELP-AI.PH$_n$ sandwiched between two panes of glass. g) Image of two 10 cm^2 devices with different solution conditions fine-tuned to immolate changes in daylight temperature of early summer (left), or midsummer (right). h) Transmittance spectra of the UnsELP-AI.PH45 at various temperatures covering wavelengths ranging from ultraviolet, visible, and near-infrared. i) Transmittance modulation of UnsELP-AI.PH45 with the layer thickness from 1 to 10 mm at 15 °C (<LCST) and 30 °C (>LCST).

hydrogels below body temperature, we assessed its potential in forming programmable porous depots for biomedical applications (Figure 6c–e),[45] which comes with the advantage that the depots can be programmed to have prolonged self-assembly, or controlled disassembly solely by altering the concentration of salt and protein concentration in the final injectable formulation (Figure 6c,d, and Videos S1 and S2, Supporting Information). To this end, we explored the stability and tissue incorporation of UnsELP-AI.PH45 with prolonged self-assembly by making injections into the wingette's subcutaneous space of a sacrificed domestic chicken. Following the 1 mL injection of UnsELP-AI.PH45, we observed a diffusion and accumulation of the compound in the subcutaneous space, resulting in the formation of an oval-shaped depot that was externally visible (Figure 6e). Subsequent X-ray computed microtomography (Micro-CT) analysis confirmed the uniform and seamless diffusion of the compound, which was associated with a high network density in the surrounding tissue.

We also explored the use of UnsELP-AI.PH_n as a self-activating compound in smart windows with the ability to self-modulate the amount of solar radiation passing through the windows as a function of external temperature without the need for human intervention, or external stimuli (Figure 6f, and Videos S3 and S4, Supporting Information). The method involved sandwiching a mm-thin layer of UnsELP-AI.PH_n between two panes of glass. The concept leverages the reversible thermoresponsive coacervation behavior of UnsELP-AI.PH_n, which remained transparent below a critical temperature T_t but condensed into an ultra-white film above T_t made from an isotropically interconnected network of low-refractive-index proteins ($n \approx 1.3$–1.5). The spectral analysis depicted in Figure 6h illustrates the transition from high transmittance at cooler temperatures to significantly reduced transmittance across the entire spectrum as temperatures approach Tt. This network scatters solar radiation across the UV, visible, and near-infrared range with low transmittance above T_t (Figure 6f–i, and Figure S27, Supporting Information). Moreover, the steep drop in transmittance observed in Figure 6i with increasing layer thickness underscores the material's efficacy in blocking solar radiation, which is particularly crucial for maintaining cooler interiors during peak sunlight hours. The UnsELP-AI.PH_n's adaptive phase behavior can alter a building's interior light, regulating indoor temperature for sustainable building design. Furthermore, the device can be customized for precise geographic locations, times of day, or months by adjusting UnsELP-AI.PH_n variants with different LCSTs, solution conditions, and device layer thicknesses. This regulatory capacity is quantitatively supported by the data in Figure 6i, where the transmittance percentage decreases with thickness, demonstrating the potential for precise tuning of light filtration. This customization is further exemplified by the variable response depicted at different temperatures in Figure 6i, providing a clear roadmap for tailoring smart window functionality to diverse climatic conditions.

3. Discussion

The emerging field of biomaterials engineering has witnessed a significant paradigm shift, with the advent of microbial biosynthesis of protein-based structural materials. However, the inherent complexity of structural proteins poses a formidable challenge that necessitates advanced toolkits to harness their full potential for real-world applications. In this work, we elucidate the challenges in replicating most structural proteins, particularly those with tandem repeat motifs that are partially disordered. Understanding the physicochemical processes governing these proteins is crucial for achieving functional and mechanical performance comparable to native biological counterparts. Our study highlights the importance of well-defined regions with conformational switchable structures, such as α-helical motifs, during material processing and properties. We acknowledged the limitations of traditional laboratory setups in replicating the evolutionary optimized physicochemical processes biomimetically. Hence, we propose a forward-looking solution—de novo design facilitated by machine learning and advanced computational modeling. This approach enables the design of arbitrary sequences with α-helical conformations Our manuscript advocates for a hybrid biomimetic/de novo design strategy that combines inspiration from nature's solutions with de novo design, thus enhancing our ability to engineer materials with tailored functionalities. Our workflow includes multiscale computational modeling and CNN deep neural network models, which have been instrumental in selecting the best-performing designs for experimental production. We encode these designs into intrinsically disordered pentapeptide repeating motifs, resulting in ELP variants with tunable self-assembled structures and phase behavior achieved through the synergistic process of de novo design of α-helical motifs and thorough adjustment of formulation parameters. This also highlights the versatility and tunability of ELP-based materials, showcasing our ability to engineer materials with specific, desired functionalities by manipulating both the peptide sequence and the formulation parameters. These findings hold promise for applications in programmable thermoresponsive injectable matrices and transmittance modulators for smart windows, indicating the practical relevance of our research. We envision the convergence of machine learning algorithms, high-throughput multiscale MD simulations, and synthetic biology to offer a compelling platform for accelerated molecular design and multiscale material optimization. This convergence promises to discover protein-based materials with custom properties and expedite the microbial revolution in biomaterials engineering. The combination of in silico design, process optimization, strain engineering, and laboratory automation promises to accelerate technological innovation and streamline workflows with remarkable speed and efficiency in the foreseeable future.

Supporting Information

Supporting Information is available from the Wiley Online Library or from the author.

Acknowledgements

This work was supported by the Academy of Finland Grant No. 348628, Jenny and Antti Wihuri Foundation (Centre for Young Synbio Scientists), the Academy of Finland Center of Excellence Program (2022-2029) in Life-Inspired Hybrid Materials (LIBER) Grant No. 346106, as well as internal funding from the VTT Technical Research Centre of Finland. The work was also financially supported by the National Science Centre, Poland, Grant No. 2018/31/D/ST5/01866. AM acknowledges financial support from the

Singapore Ministry of Education (MOE) through an Academic Research (AcRF) Tier 3 grant (Grant No. MOE 2019-T3-1-012) and from the strategic initiative on biomimetic and sustainable materials (IBSM) at Nanyang Technological University (NTU). The authors would like to acknowledge Omar Masrouji and Marius Hope for their assistance during the project. This work acknowledges the provision of facilities and technical support by Aalto University at the OtaNano Nanomicroscopy Center (Aalto-NMC). The authors wish to acknowledge CSC – IT Center for Science, Finland, as well as Poland's high-performance computing infrastructure PLGrid (HPC Centers: ACK Cyfronet AGH) grant no. PLG/2023/016229, for providing computational resources.

Conflict of Interest

The authors declare no conflict of interest.

Author Contributions

T.L. and A.K. contributed equally to this work. All authors contributed equally to this research by designing the experiments, interpreting the results, writing, editing, revising, and approving of the final version of the manuscript.

Data Availability Statement

The data that support the findings of this study are available from the corresponding author upon reasonable request.

Keywords

computational modeling, de novo design, Î±-helical conformation, machine learning, protein engineering

Received: November 17, 2023
Revised: March 28, 2024
Published online: May 11, 2024

[1] P. Mohammadi, A. S. Aranko, C. P. Landowski, O. Ikkala, K. Jaudzems, W. Wagermaier, M. Linder, *Sci. Adv.* **2019**, *5*, eaaw2541.
[2] P. Mohammadi, J.-A. Gandier, N. Nonappa, W. Wagermaier, A. Miserez, M. Penttilä, *Advanced Materials* **2021**, *33*, 2102658.
[3] S. Ling, D. L. Kaplan, M. J. Buehler, *Nat. Rev. Mater.* **2018**, *3*, 18016.
[4] F. Barthelat, Z. Yin, M. J. Buehler, *Nat. Rev. Mater.* **2016**, *1*, 16007.
[5] A. Miserez, J. Yu, P. Mohammadi, *Chem. Rev.* **2023**, *123*, 2049.
[6] S. Amini, M. Tadayon, J. J. Loke, A. Kumar, D. Kanagavel, H. Le Ferrand, M. Duchamp, M. Raida, R. M. Sobota, L. Chen, *Proc. Natl. Acad. Sci. USA* **2019**, *116*, 8685.
[7] Y. Tan, S. Hoon, P. A. Guerette, W. Wei, A. Ghadban, C. Hao, A. Miserez, J. H. Waite, *Nat. Chem. Biol.* **2015**, *11*, 488.
[8] F. Vollrath, D. P. Knight, *Nature* **2001**, *410*, 541.
[9] P. A. Guerette, S. Hoon, Y. Seow, M. Raida, A. Masic, F. T. Wong, V. H. B. Ho, K. W. Kong, M. C. Demirel, A. Pena-Francesch, *Nat. Biotechnol.* **2013**, *31*, 908.
[10] M. S. Packer, D. R. Liu, *Nat. Rev. Genet.* **2015**, *16*, 379.
[11] M. Amiram, F. G. Quiroz, D. J. Callahan, A. Chilkoti, *Nat. Mater.* **2011**, *10*, 141.
[12] S. Roberts, T. S. Harmon, J. L. Schaal, V. Miao, K. J. Li, A. Hunt, Y. Wen, T. G. Oas, J. H. Collier, R. v Pappu, *Nat. Mater.* **2018**, *17*, 1154.
[13] D. S. Fudge, K. H. Gardner, V. T. Forsyth, C. Riekel, J. M. Gosline, *Biophys. J.* **2003**, *85*, 2015.
[14] A. Miserez, S. S. Wasko, C. F. Carpenter, J. H. Waite, *Nat. Mater.* **2009**, *8*, 910.
[15] T. Priemel, E. Degtyar, M. N. Dean, M. J. Harrington, *Nat. Commun.* **2017**, *8*, 14539.
[16] F. Jehle, E. Macías-Sánchez, P. Fratzl, L. Bertinetti, M. J. Harrington, *Nat. Commun.* **2020**, *11*, 862.
[17] H.-J. Jin, D. L. Kaplan, *Nature* **2003**, *424*, 1057.
[18] G. Askarieh, M. Hedhammar, K. Nordling, A. Saenz, C. Casals, A. Rising, J. Johansson, S. D. Knight, *Nature* **2010**, *465*, 236.
[19] R. Chowdhury, N. Bouatta, S. Biswas, C. Floristean, A. Kharkar, K. Roy, C. Rochereau, G. Ahdritz, J. Zhang, G. M. Church, P. K. Sorger, M. AlQuraishi, *Nat. Biotechnol.* **2022**, *40*, 1617.
[20] N. Ferruz, B. Höcker, *Nat. Biotechnol.* **2022**, *40*, 171.
[21] I. D. Lutz, S. Wang, C. Norn, A. Courbet, A. J. Borst, Y. T. Zhao, A. Dosey, L. Cao, J. Xu, E. M. Leaf, C. Treichel, P. Litvicov, Z. Li, A. D. Goodson, P. Rivera-Sánchez, A. M. Bratovianu, M. Baek, N. P. King, H. Ruohola-Baker, D. Baker, *Science* **2023**, *380*, 266.
[22] P. Bradley, K. M. S. Misura, D. Baker, *Science* **2005**, *309*, 1868.
[23] B. I. M. Wicky, L. F. Milles, A. Courbet, R. J. Ragotte, J. Dauparas, E. Kinfu, S. Tipps, R. D. Kibler, M. Baek, F. DiMaio, X. Li, L. Carter, A. Kang, H. Nguyen, A. K. Bera, D. Baker, *Science* **2022**, *378*, 56.
[24] A. Ljubetič, F. Lapenta, H. Gradišar, I. Drobnak, J. Aupič, Ž. Strmšek, D. Lainšček, I. Hafner-Bratkovič, A. Majerle, N. Krivec, M. Benčina, T. Pisanski, T. Ć Veličković, A. Round, J. M. Carazo, R. Melero, R. Jerala, *Nat. Biotechnol.* **2017**, *35*, 1094.
[25] S. M. Mithieux, A. S. Weiss, *Adv. Protein Chem.* **2005**, *70*, 437.
[26] R. P. Visconti, J. L. Barth, F. W. Keeley, C. D. Little, *Matrix Biol.* **2003**, *22*, 109.
[27] L. D. Muiznieks, A. S. Weiss, F. W. Keeley, *Biochem. Cell Biol.* **2010**, *88*, 239.
[28] S. E. Reichheld, L. D. Muiznieks, F. W. Keeley, S. Sharpe, *Proc. Natl. Acad. Sci.* **2017**, *114*, E4408.
[29] S. Roberts, M. Dzuricky, A. Chilkoti, *FEBS Lett.* **2015**, *589*, 2477.
[30] S. Roberts, V. Miao, S. Costa, J. Simon, G. Kelly, T. Shah, S. Zauscher, A. Chilkoti, *Nat. Commun.* **2020**, *11*, 1342.
[31] L. D. Muiznieks, S. Sharpe, R. Pomès, F. W. Keeley, *J. Mol. Biol.* **2018**, *430*, 4741.
[32] L. D. Muiznieks, J. T. Cirulis, A. van der Horst, D. P. Reinhardt, G. J. L. Wuite, R. Pomès, F. W. Keeley, *Matrix Biol.* **2014**, *36*, 39.
[33] B. Li, V. Daggett, *J. Muscle Res. Cell Motil.* **2002**, *23*, 561.
[34] A. W. Senior, R. Evans, J. Jumper, J. Kirkpatrick, L. Sifre, T. Green, C. Qin, A. Žídek, A. W. R. Nelson, A. Bridgland, H. Penedones, S. Petersen, K. Simonyan, S. Crossan, P. Kohli, D. T. Jones, D. Silver, K. Kavukcuoglu, D. Hassabis, *Nature* **2020**, *577*, 706.
[35] J. Jumper, R. Evans, A. Pritzel, T. Green, M. Figurnov, O. Ronneberger, K. Tunyasuvunakool, R. Bates, A. Žídek, A. Potapenko, A. Bridgland, C. Meyer, S. A. A. Kohl, A. J. Ballard, A. Cowie, B. Romera-Paredes, S. Nikolov, R. Jain, J. Adler, T. Back, S. Petersen, D. Reiman, E. Clancy, M. Zielinski, M. Steinegger, M. Pacholska, T. Berghammer, S. Bodenstein, D. Silver, O. Vinyals, et al., *Nature* **2021**, *596*, 583.
[36] K. Manalastas-Cantos, P. V. Konarev, N. R. Hajizadeh, A. G. Kikhney, M. V. Petoukhov, D. S. Molodenskiy, A. Panjkovich, H. D. T. Mertens, A. Gruzinov, C. Borges, C. M. Jeffries, D. I. Svergun, D. Frankea, *J. Appl. Crystallogr.* **2021**, *54*, 343.
[37] P. C. Chen, J. S. Hub, *Biophys. J.* **2014**, *107*, 435.
[38] A. Micsonai, F. Wien, L. Kernya, Y. H. Lee, Y. Goto, M. Réfrégiers, J. Kardos, *Proc. Natl. Acad. Sci. U. S. A.* **2015**, *112*, E3095.
[39] D. Bracha, M. T. Walls, C. P. Brangwynne, *Nat. Biotechnol.* **2019**, *37*, 1435.
[40] P. Mohammadi, J. Christopher, G. Beaune, P. Engelhardt, A. Kamada, J. V. I. Timonen, T. P. J. Knowles, M. Penttila, M. B. Linder, *J. Colloid Interface Sci.* **2020**, *560*, 149.
[41] B. A. Krajina, B. L. LeSavage, J. G. Roth, A. W. Zhu, P. C. Cai, A. J. Spakowitz, S. C. Heilshorn, *Sci. Adv.* **2021**, *7*, eabe1969.

[42] L. Jawerth, E. Fischer-Friedrich, S. Saha, J. Wang, T. Franzmann, X. Zhang, J. Sachweh, M. Ruer, M. Ijavi, S. Saha, J. Mahamid, A. A. Hyman, F. Jülicher, *Science* **2020**, *370*, 1317.
[43] L.-W. Chang, T. K. Lytle, M. Radhakrishna, J. J. Madinya, J. Vélez, C. E. Sing, S. L. Perry, *Nat. Commun.* **2017**, *8*, 1273.
[44] P. Batys, D. Fedorov, P. Mohammadi, L. Lemetti, M. B. Linder, M. Sammalkorpi, *Biomacromolecules* **2021**, *22*, 690.
[45] D. L. Nettles, A. Chilkoti, L. A. Setton, *Adv. Drug Deliv. Rev.* **2010**, *62*, 1479.